



An electrochemical–thermal model based on dynamic responses for lithium iron phosphate battery



Jie Li, Yun Cheng, Ming Jia*, Yiwei Tang, Yue Lin, Zhian Zhang, Yexiang Liu

School of Metallurgy and Environment, Central South University, Changsha 410083, China

HIGHLIGHTS

- A model based on dynamic responses for LiFePO₄ battery is developed.
- Effects of current collectors on LiFePO₄ battery are considered in this model.
- Dynamic analysis for pulse behavior and electrochemical rates are conducted.
- Endothermic and exothermic phenomena in different discharge rates are discussed.

ARTICLE INFO

Article history:

Received 11 October 2013

Received in revised form

25 December 2013

Accepted 1 January 2014

Available online 9 January 2014

Keywords:

Electrochemical–thermal model

Dynamic responses

Lithium iron phosphate battery

Pulse behavior

Thermal behavior

ABSTRACT

An electrochemical–thermal model is developed to predict electrochemical and thermal behaviors of commercial LiFePO₄ battery during a discharging process. A series of temperatures and lithium ion concentrations dependent parameters relevant to the reaction rate and Li⁺ transport are employed in this model. A non-negligible contribution of current collectors to the average heat generation of the battery is considered. Simulation results on rate capability and temperature performance show good agreement with the literature data. The behavior of Li⁺ distribution at pulse-relaxation discharge, the variation of electrochemical reaction rate and thermal behavior at a constant current discharge are studied. Results of pulse-relaxation discharge describe the dynamic change of Li⁺ concentration distribution in liquid and solid phases, which is helpful to analysis the polarization of the battery. In constant current discharge processes, the electrochemical reaction rate of positive electrode has a regular change with the time and the position in the electrode. When discharge finished, there is still a part of the LiFePO₄ material has not been adequately utilized. At low rate, the discharge process accompanies endothermic and exothermic processes. With the rate increasing, the endothermic process disappears gradually, and only exothermic process left at high rate.

© 2014 Elsevier B.V. All rights reserved.

1. Introduction

Lithium ion battery is nowadays one of the most popular energy storage devices due to high energy, power density and cycle life characteristics [1,2]. It has been known that the overall performance of batteries not only depends on electrolyte and electrode materials, but also depends on operation conditions and choice of physical parameters [3]. Designers need an understanding on thermodynamic and kinetic characteristics of batteries that is costly and time-consuming by experimental methods. Conversely, numerical modeling and simulation for batteries are economic, which can provide guidelines for design in a short time [4], and

information during the electrochemical and transport process. For example, the local electric potential and ion concentrations throughout the porous electrodes can be calculated while the data cannot be obtained experimentally [5,6].

The accuracy of numerical modeling and simulation of electrochemical and thermal behavior relies on the model construction and the parameters applied during simulation [7]. The most famous and practical model for lithium ion battery is the porous electrode model [8,9], which was based on the porous electrode theory containing charge transfer kinetics at reaction sites, species and charge conservations. It was combined with an energy conservation equation by Newman and Pals [10,11], and was developed as an electro-thermal model, which made it possibly simulate and predict the interaction between temperature and electrochemical reaction of batteries. Previously, the electrochemical models and

* Corresponding author.

E-mail address: jiamingsunmoon@aliyun.com (M. Jia).

Nomenclature

List of symbols

A_{cell}	area of the positive electrode (both sides) (m^2)
$c_{1,i}$	lithium in active material (mol m^{-3})
$C_{1,\text{max},i}$	maximum concentration (mol m^{-3})
$C_{1,\text{surf},i}$	Li^+ concentration on the surface of active material particles (mol m^{-3})
$C_{p,i}$	heat capacity (J (kg K)^{-1})
$D_{1,i}$	solid phase diffusivity ($\text{m}^2 \text{s}^{-1}$)
$D_{10,i}$	reference solid phase diffusivity ($\text{m}^2 \text{s}^{-1}$)
$E_{a,D,i}$	diffusion active energy (kJ mol^{-1})
$E_{a,k,i}$	reaction active energy (kJ mol^{-1})
h	heat transfer coefficient ($\text{W m}^{-2} \text{K}^{-1}$)
I	current (A)
I_{app}	cell current density related to A_{cell} (A m^{-2})
$j_{0,i}$	exchange current density (A m^{-2})
$j_{\text{loc},i}$	local current density (A m^{-2})
$k_{0,i}$	reaction rate constant ($\text{m}^{2.5} \text{mol}^{-0.5} \text{s}^{-1}$)
k_i	thermal conductivity (W (m K)^{-1})
L_i	thickness of component (m)
Q_{act}	active heat generation (J m^{-3})
Q_{ohm}	ohmic heat generation (J m^{-3})
Q_{rea}	reaction heat generation (J m^{-3})
r	radius distance variable of particle (m)
R_i	characteristic radius of electrode particles (m)
$S_{a,i}$	specific surface area (m^{-1})
$\text{SOC}_{0,i}$	initial state of charge
t	time (s)

t^+	Li^+ transference number
T	absolute temperature (K)
T_{amb}	ambient temperature (K)
U_i	open circuit voltage (V)
v	thermodynamic factor relating to electrolyte activity
x	distance from half negative foil along negative-positive direction (m)

Greek letters

$\alpha_{a,i}$	transfer coefficient for anodic current
$\alpha_{c,i}$	transfer coefficient for cathodic current
$\varepsilon_{1,i}$	active material volume fraction
$\varepsilon_{2,i}$	volume fraction
φ_i	electric potential (V)
γ_i	Bruggeman exponent
k	ionic or electronic conductivity (S m^{-1})
ρ_i	density (kg m^{-3})
σ_i	solid phase conductivity (S m^{-1})

Subscripts and superscripts

0	initial or equilibrated state
1	solid phase
2	liquid phase
amb	ambient temperature
n	negative electrode
p	positive electrode
irr	irreversible
re	reversible
s	separator

electrochemical thermal models were built for simulating the cathode materials of lithium ion battery, such as LiCoO_2 , LiMn_2O_4 or $\text{Li}(\text{NiCoMn})\text{O}_2$ [12–18]. Later, based on the observation of a phase change occurred in the LiFePO_4 cathode during the lithiated and unlithiated process [19,20], Srinivasan [21] developed a model that accounted for the phase change with the shrinking core, and investigated the cause for the low power capability of the materials. The other models without special features about the two-phase process were also founded for further qualitative analysis [22–31]. For instance, Wang [22] analyzed the effect of local current density on electrode design for the LiFePO_4 battery. Ye [23] developed an electro-thermal cycle life model by incorporating the dominant capacity fading mechanism to investigate the capacity fading effect on the performance. Gerver [24] and Christian Hellwig [25] gave a multidimensional modeling framework for simulating coupled thermal and electrochemical phenomena that are critical for safety, durability and design optimization studies. These models demonstrated that the porous electrode theory can be used to simulate a LiFePO_4 battery system without considering the phase change.

In the previous work [8–31], the computational domains were divided into three parts, named negative electrode, separator and positive electrode, but the current collectors of a battery were neglected. Because a rate of the heat generation is an average value obtained through dividing the total heat generation by the cell volume, about 10% of the cell volume comes from the current collectors, indicating that the contribution of the collectors to the heat generation rate cannot be neglected.

Besides, the material properties treated as parameters also have an important influence on the accuracy of the simulation [7]. During the discharge process, lithium ions deintercalate from the negative porous electrode, then transfer through separator and

intercalate into the positive electrode, resulting in changes of temperature and lithium ion concentrations in the solid and liquid phases that may affect the diffusion coefficient, ionic conductivity, ion transference number as well as the reaction rate constant [24,32–34]. Therefore, it is necessary to rectify dynamically these parameters during a simulation.

In this study, we develop an electrochemical thermal model for a LiFePO_4 battery by considering the current collectors into the computational domain, dynamic responses in lithium ion concentration, and temperature as parameters during the discharge process. By comparing experimental results with simulation at different operating temperatures and discharge rates, this model can be used to study the dynamic evolution for pulses, relaxation behavior, electrochemical reaction and thermal behavior at a constant discharge rate in lithium iron phosphate battery.

2. Model development

2.1. Model assumption and simulation domain

This electrochemical–thermal model for a LiFePO_4 battery is developed based on the porous electrode model [8,9]. The active materials of solid electrodes are treated as homogenous media, and are comprised with spherical particles. Since the current collectors play an important role in electron and heat transferring, the current collectors are considered as a computing domain.

Fig. 1 shows a schematic computational domain of one-dimensional (1D) battery model [8,9]. Because both positive and negative current collectors have two sides contacting and reacting with electrolyte, we take a half of their thickness into simulation domain in order to accurately calculate the current flow and the

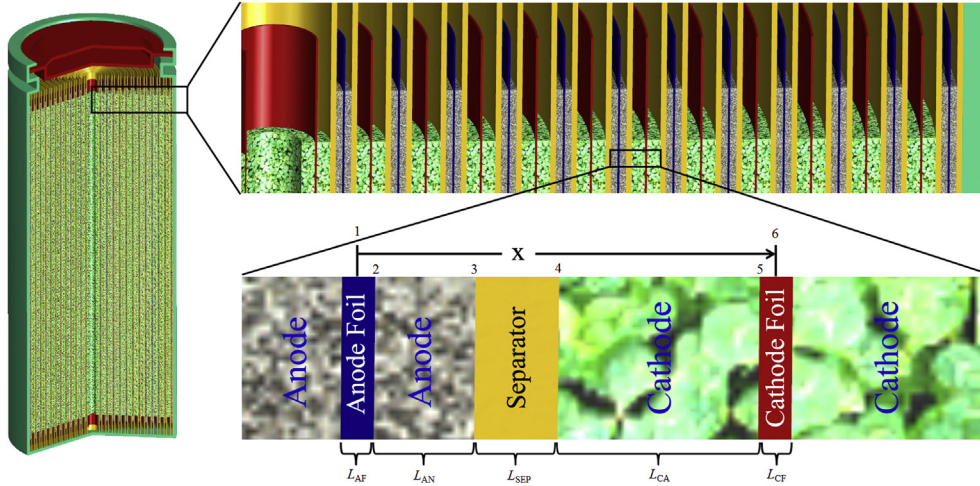


Fig. 1. Schematic diagram of lithium iron phosphate battery and computational domain.

heat generation. There are six boundaries in the model. Four inner boundaries (anode current collector/anode interface boundaries 2, anode/separator interface boundaries 3, separator/cathode interface boundaries 4 and cathode/cathode current collector interface boundaries 5) and two external boundaries (anode current collector external-face boundary 1 and cathode current collector external-face boundary 6) are shown in Fig. 1.

2.2. Electrochemical part

2.2.1. Electronic charge conservation

(a) Solid phase. There is a double layer capacitance at the interface between the active materials and electrolyte [35]. The capacitance can store additional energy and smooth the abrupt change of the cell voltage caused by the short-time pulses passing through a cell. However, the capacitance was seldom considered in the previous models [35]. Small modification in the electronic charge conservation is required to account of the double layer. Electronic charge conservation for solid phase can be expressed as follows:

$$\nabla \cdot (-\sigma_c \nabla \phi_c) = -J_i \quad (1)$$

$$\nabla \cdot (-k_1^{\text{eff}} \nabla \phi_1) = -S_{a,i} \left(j_{\text{loc},i} + C_{\text{dl}} \left(\frac{\partial \phi_1}{\partial t} - \frac{\partial \phi_2}{\partial t} \right) \right) \quad (2)$$

$$S_{a,i} = \frac{3\varepsilon_{1,i}}{r_{p,1}}; k_1^{\text{eff}} = k_1 \varepsilon_1^{\gamma_1} \quad (3)$$

where ϕ_c is arbitrarily set to zero at boundary 1; at boundary 6, the charge flux is set to equal the average current density of the battery, which is expressed as Eq. (4); at boundary 3 and boundary 4, there is no charge flux, which is expressed as Eq. (5) and the boundary condition is set as isolation.

$$\phi_c|_{x=0} = 0; -\sigma_c \nabla \phi_c|_{x=L_{\text{ncc}}+L_n+L_s+L_p+L_{\text{pcc}}} = -I_{\text{app}} \quad (4)$$

$$-k_1^{\text{eff}} \nabla \phi_1|_{x=L_{\text{ncc}}+L_n} = 0; -k_1^{\text{eff}} \nabla \phi_1|_{x=L_{\text{ncc}}+L_n+L_s} = 0 \quad (5)$$

(b) Solution phase. According to the concentrated solution theory, the governing equation for electronic charge conservation in solution phase is expressed as:

$$\nabla \cdot \left\{ k_2^{\text{eff}} \left[-\nabla \phi_2 + \frac{2RT}{F} \left[1 + \frac{\partial \ln f}{\partial \ln c_2} \right] (1 - t_+) \frac{\nabla c_2}{c_2} \right] \right\} = S_{a,i} j_{\text{loc},i} \quad (6)$$

$$k_2^{\text{eff}} = k_2 \varepsilon_2^{\gamma_2} \quad (7)$$

Liquid-junction potential is introduced in Eq. (6) with expression

$$K_{\text{junc}} = \frac{2RT}{F} \left[1 + \frac{\partial \ln f}{\partial \ln c_2} \right] (1 - t_+) = \frac{2RT}{F} \nu \quad (8)$$

The parameter ν is the thermodynamic factor relating to electrolyte activity, and it is concentration and temperature dependent.

There is no flux at external boundaries (boundary 1 and boundary 6), which is expressed as Eq. (9); the parameter ϕ_2 is taken to be continuous at boundary 2 and boundary 5.

$$\frac{\partial \phi_2}{\partial x} \Big|_{x=L_{\text{ncc}}} = \frac{\partial \phi_2}{\partial x} \Big|_{x=L_{\text{ncc}}+L_n+L_s+L_p} = 0 \quad (9)$$

2.2.2. Mass conservation

(a) Solid phase. The mass conservation of lithium ions in an intercalation particle of the electrode active material is described by Fick's law. The parameter r is the distance from the center of solid sphere, the mass transport within solid phase in spherical coordinates can be described as:

$$\frac{\partial c_{1,i}}{\partial t} = \frac{D_{1,i}}{r^2} \left[\frac{\partial}{\partial r} \left(r^2 \frac{\partial c_{1,i}}{\partial r} \right) \right] = D_{1,i} \left(\frac{2}{r} \frac{\partial c_{1,i}}{\partial r} + \frac{\partial^2 c_{1,i}}{\partial r^2} \right) \quad (10)$$

Let the variable τ equal to r/R_i , the Eq. (10) can be described as

$$\tau^2 R_i \frac{\partial c_{1,i}}{\partial t} = \frac{D_{1,i}}{R_i} \left[\frac{\partial}{\partial \tau} \left(\tau^2 \frac{\partial c_{1,i}}{\partial \tau} \right) \right] \quad (11)$$

The parameter R_i is the particle radius. There is no species source at the center of sphere, so $\partial c_{1,i}/\partial \tau|_{\tau=0} = 0$. The Li^+ concentration on the surface of the particles is coupled to the concentration and flux in the 1D model for the charge and material transport in the electrolyte.

(b) Solution phase. Solution phase mass conservation for LiF_6 dissolved in the liquid phase

$$\varepsilon_2 \frac{dc_2}{dt} + \nabla \cdot \left\{ -D_2^{\text{eff}} \nabla c_2 \right\} = \frac{S_{a,i} j_{\text{loc},i}}{F} (1 - t_+) \quad (12)$$

$$D_2^{\text{eff}} = D_2 \varepsilon_2^{\gamma_2} \quad (13)$$

The flux of liquid species is arbitrarily set to zero at boundary 2 and boundary 5, liquid species flux and species concentration at boundary 3 and boundary 4 are taken to be continuous.

2.2.3. Electrochemical kinetics

The local current per active material area is calculated using the Butler–Volmer equation:

$$j_{\text{loc},i} = j_{0,i} \left\{ \exp \left[\frac{\alpha_{a,i} \eta_i F}{RT} \right] - \exp \left[\frac{-\alpha_{c,i} \eta_i F}{RT} \right] \right\} \quad (14)$$

The parameter $j_{\text{loc},i}$ is driven by over-potential, the parameter η_i is defined as the difference between solid and electrolyte phase potentials minus U_i .

$$\eta_i = \phi_{1,i} - \phi_{2,i} - U_i \quad (15)$$

The parameter U_i is the thermodynamic equilibrium potential of the solid phase and is taken to be a function of the local SOC on the surface of active particles.

The temperature-dependent open circuit potentials of positive and negative electrodes are approximated by Taylor's first order expansion around a reference temperature:

$$U_i = U_{\text{ref},i} + (T - T_{\text{ref}}) \frac{dU_i}{dT} \quad (16)$$

The parameter $U_{\text{ref},i}$ is the open circuit potential under the reference temperature.

In Eq. (14), exchange current density, $j_{0,i}$, connects concentrations in both solid and liquid phase:

$$j_{0,i} = F k_i c_2^{\alpha_{a,i}} \left(c_{1,\text{max},i} - c_{1,\text{surf},i} \right)^{\alpha_{a,i}} c_{1,\text{surf},i}^{\alpha_{c,i}} \quad (17)$$

The parameter k_i is the reaction rate, considered temperature dependent in this paper. The parameters α_a and α_c are the anodic and cathodic transfer coefficients, respectively.

The outputs of the model are the cell potential, current density distribution, species and concentrations distributions, and the cell potential is derived by following expression:

$$E = \phi_1|_{x=L_{\text{ncc}}+L_n+L_s+L_p+L_{\text{pcc}}} - \phi_1|_{x=0} \quad (18)$$

2.3. Energy conservation

The heat generation is modeled with the local heat generation model of Rao and Newman [36] using the formulation of Gu and Wang [37]. According to the position of heat generation, the total heat generation is the summation of heat generated in the two electrodes, separator and current collectors. The summary of the heat generation mechanisms is listed in Table 1.

According to the type of the heat generation, there are three parts of heat sources during the charge or discharge processes, including reaction heat, Q_{rea} , due to entropy change during the discharge; ohmic heat, Q_{ohm} , due to the ohmic potential drop and active polarization heat, Q_{act} , due to the electrochemical reaction polarization between active material particle surface and the electrolyte.

Reaction heat generation is:

$$Q_{\text{rea}} = S_{a,i} j_{\text{loc},i} T \frac{dU_i}{dT} \quad (24)$$

Ohmic heat generation is:

$$Q_{\text{ohm}} = q_{i,(2)} + q_{i,(3)} + q_s + q_{i,c} \quad (25)$$

Active heat generation is:

$$Q_{\text{act}} = S_{a,i} j_{\text{loc},i} (\phi_{1,i} - \phi_{2,i} - U_i) \quad (26)$$

Active heat Q_{act} and ohmic Q_{ohm} are irreversible, while reaction heat Q_{rea} is reversible.

$$Q_{\text{irr}} = Q_{\text{ohm}} + Q_{\text{act}} \quad (27)$$

$$Q_{\text{re}} = Q_{\text{rea}} \quad (28)$$

The energy conservation in lithium ion battery is shown as follows:

$$\rho_i C_{p,i} \frac{\partial T}{\partial t} + \nabla \cdot (-k_i \nabla T) = Q_{\text{irr}} + Q_{\text{re}} \quad (29)$$

The parameters ρ_i , $C_{p,i}$ and k_i are density, heat capacity and thermal conductivity, respectively.

According to Newton's cooling law and radiation law, the boundary condition for energy conservation is expressed as:

$$-\lambda \nabla T = -h(T_{\text{amb}} - T) - \varepsilon \sigma (T_{\text{amb}}^4 - T^4) \quad (30)$$

The parameter λ is thermal conductivity of stainless steel case, h is natural convection heat transfer coefficient ($h = 7.17 \text{ W m}^{-2} \text{ K}^{-1}$ [38]), T_{amb} is ambient temperature, and ε is the blackness of the battery surface ($\varepsilon = 0.8$ [38]).

3. Model parameters and model validation

3.1. Battery parameters and thermal properties

The physical properties of battery components and battery design parameters are summarized in Tables 2 and 3, respectively.

3.2. Dynamic parameters

The dynamic response of battery properties is attributed to the change of temperature and lithium-ion concentration during the discharge and charge processes. It is considered for eight sets of physical properties. These are (1) $k_{0,i}$, the reaction rate constant; (2) $D_{1,i}$, the diffusion coefficient of Li^+ in the solid active particles; (3) open circuit potential (OCP) of the electrodes; (4) D_2 , the diffusion coefficient of Li^+ in the electrolyte; (5) k_2 , the electrolyte ionic conductivity; (6) v , the thermodynamic factor relating to electrolyte activity; (7) t^+ , the Li^+ transference number; (8) σ_c , current collector electrical conductivity.

3.2.1. Dynamic variables related to electrodes

3.2.1.1. Electrode kinetics properties. The dynamic temperature dependences of $D_{1,i}$ follow the Arrhenius equation. However, the LFP electrode exhibited significantly higher utilization on charging than on discharging at the same current density [39]. This asymmetry was ascribed to the different transport limitation between the fully charged and discharged states [40]. To account for this asymmetry, an empirical equation is used for the solid-state Li^+ diffusion coefficient that is dependent on the average lithium ion concentration of particles [27]:

Table 1
Heat generation mechanism in a cell.

Heat generation mechanism	Equation
<i>Porous electrode</i>	
(1). Electrochemical interface	$q_{i,(1)} = S_{a,i} j_{loc,i} \left(T \frac{dU_i}{dT} + \phi_{1,i} - \phi_{2,i} - U_i \right)$ (19)
(2). Electrical ohmic heat	$q_{i,(2)} = \sigma_i^{\text{eff}} \nabla \phi_{1,i} \cdot \nabla \phi_{1,i}$ (20)
(3). Ionic ohmic heat	$q_{i,(3)} = k_2^{\text{eff}} \nabla \phi_{2,i} \cdot \nabla \phi_{2,i} + \frac{2RTk_2^{\text{eff}}}{F} (t_+ - 1) \left[1 + \frac{\partial \ln f}{\partial \ln c_{2,i}} \right] \cdot \nabla (\ln c_{2,i}) \cdot \nabla \phi_{2,i}$ (21)
<i>Separator</i>	
Ionic ohmic heat	$q_s = k_2^{\text{eff}} \nabla \phi_2 \cdot \nabla \phi_2 + \frac{2RTk_2^{\text{eff}}}{F} (t_+ - 1) \left[1 + \frac{\partial \ln f}{\partial \ln c_2} \right] \cdot \nabla (\ln c_2) \cdot \nabla \phi_2$ (22)
<i>Current collector</i>	
Electrical ohmic heat	$q_{i,c} = \sigma_{i,c} \nabla \phi_{i,c} \cdot \nabla \phi_{i,c}$ (23)

Subscript i = n or p for a negative or a positive electrode.

$$D_{1,p} = \frac{1.18 \times 10^{-18}}{(1+y)^{1.6}} \quad (31)$$

In this study, we take a combination of the Arrhenius equation and Eq. (31) into the formula for the $D_{1,p}$, which is expressed as:

$$D_{1,p} = \frac{1.18 \times 10^{-18}}{(1+y)^{1.6}} \exp \left(-\frac{E_{1,D,p}}{R} \left(\frac{1}{T} - \frac{1}{298.15} \right) \right) \quad (32)$$

The state of charge (SOC) and temperature also affect $k_{0,i}$ and $D_{1,n}$, but duo to lack of data, the SOC is not considered. $k_{1,i}$ and $D_{1,n}$ are expressed by Eqs. (33)–(35) followed the Arrhenius formula [41].

$$D_{1,n} = 3.9 \times 10^{-14} \exp \left(-\frac{E_{1,D,n}}{R} \left(\frac{1}{T} - \frac{1}{298.15} \right) \right) \quad (33)$$

$$k_{1,n} = 3 \times 10^{-11} \exp \left(-\frac{E_{1,k,n}}{R} \left(\frac{1}{T} - \frac{1}{298.15} \right) \right) \quad (34)$$

$$k_{1,p} = 1.4 \times 10^{-12} \exp(-3y) \exp \left(-\frac{E_{1,k,p}}{R} \left(\frac{1}{T} - \frac{1}{298.15} \right) \right) \quad (35)$$

Table 2
Thermal properties of battery components.

Materials	Density (kg m ⁻³)	Heat capacity (J (kg K) ⁻¹)	Thermal conductivity, (W (m K) ⁻¹)	Electrical conductivity, (S m ⁻¹)
Negative electrode	2223	641	1.04	100
Positive electrode	1500	800	1.48	0.5
Separator	900	1883	0.5	—
Electrolyte	1210	1518	0.099	Eqs. (42) and (43)
Copper foil	8700	396	398	$-0.048897^3 + 54.657^2$ $- 218.007 + 3.52 \times 10^6$ (s cm ⁻¹)
Aluminum foil	2700	897	237	$-0.03257^3 + 37.077^2$ $- 15.0007 + 2.408$ $\times 10^6$ (s cm ⁻¹)
Stainless steel case	7500	460	14	—

The parameters $E_{1,D,p}$ and $E_{1,D,n}$ are the activation energy for diffusion of lithium respectively in the positive and negative electrodes, ($E_{1,D,p} = 35$ kJ mol⁻¹ [23,28], $E_{1,D,n} = 35$ kJ mol⁻¹ [23,42]). The parameters $E_{1,k,p}$ and $E_{1,k,n}$ are the activation energy for the rate constant of the positive and negative electrodes, respectively ($E_{1,k,p} = 20$ kJ mol⁻¹ [23,43], $E_{1,k,n} = 30$ kJ mol⁻¹ [23,28]).

3.2.1.2. Electrode thermodynamics properties. The open circuit potentials of the positive electrode U_p and the negative electrode U_n are a function of local SOC on the surface of active particles. U_p and U_n come from Ref. [28], which are expressed by Eqs. (36) and (37).

$$U_{\text{ref}} = 3.4323 - 0.4828 \exp \left(-80.2493(1-y)^{1.3198} \right) - 3.2474 \times 10^{-6} \exp \left(20.2645(1-y)^{3.8003} \right) + 3.2482 \times 10^{-6} \exp \left(20.2646(1-y)^{3.7995} \right) \quad (36)$$

$$U_{\text{ref}} = 0.6379 + 0.5416 \exp(-305.5309x) + 0.044 \tanh \left(\frac{x-0.1958}{0.1088} \right) - 0.1978 \tanh \left(\frac{x-1.0571}{0.0854} \right) - 0.6875 \tanh \left(\frac{x-0.0117}{0.0529} \right) - 0.0175 \tanh \left(\frac{x-0.5692}{0.0875} \right) \quad (37)$$

Entropy change in electrodes is $\Delta S = nF(dU/dT)$. dU_p/dT and dU_n/dT are the entropy changes of lithium iron phosphate positive electrode and the negative electrode, respectively. Their curves [44,45] are as shown in Fig. 2, and are expressed by Eqs. (38) and (39).

$$\frac{dU_p}{dT} = -0.35376y^8 + 1.3902y^7 - 2.2585y^6 + 1.9635y^5 - 0.98716y^4 + 0.28857y^3 - 0.046272y^2 + 0.0032158y - 1.9186 \times 10^{-5} \quad (38)$$

Table 3Critical battery parameters used in baseline for a 2.3 Ah LiFePO₄ cylindrical 26650 type battery.

Quantity	Negative electrode	Positive electrode	Separator	Electrolyte	Copper foil	Aluminum foil
<i>Design specifications (geometry and volume fractions)</i>						
$A_{\text{cell}}(\text{m}^2)$	0.1694					
$\epsilon_{1,i}$	0.55	0.43	—			
$\epsilon_{2,i}$	0.33	0.332	0.54			
L_i (μm)	34	70	25		6.2 (half thickness)	10 (half thickness)
R_i (μm)	0.0365	3.5				
<i>Lithium ion concentrations</i>						
$c_{\text{ini},2}$ (mol m^{-3})				1200		
c_{max} (mol m^{-3})	31,370	22,806				
$c_{\text{ini},1}$ (mol m^{-3})	31,370 * 0.86	22,806 * 0.022				
<i>Kinetic and transport properties</i>						
$a_{a,i}, a_{c,i}$	0.5	0.5				
γ_i	1.5	1.5	1.5			
D_2 ($\text{m}^2 \text{s}^{-1}$)				Eq. (40)		
C_{dl} (F m^{-2})	0.2	0.2				
$D_{1,i}$ ($\text{m}^2 \text{s}^{-1}$)	Eq. (33)	Eq. (32)				
k_1 ($\text{m}^{2.5} \text{mol}^{-0.5} \text{s}^{-1}$)	Eq. (34)	Eq. (35)				
$E_{a,k,i}$ (J mol^{-1})	20,000	30,000				
k_1 (S m^{-1})	100	0.5				
k_2 (S m^{-1})				Eqs. (42) and (43)		
σ_c						
t^+				Eq. (44)		
v				Eq. (41)		
<i>Constant quantity</i>						
T_{ref} (K)	298.15					
F (C mol^{-1})	96,487					

$$\frac{dU_n}{dT} = 344.1347148 \times \frac{\exp(-32.9633287x + 8.316711484)}{1 + 749.0756003 \exp(-34.79099646x + 8.887143624) - 0.8520278805x + 0.362299229x^2 + 0.2698001697} \quad (39)$$

3.2.2. Dynamic variables related to lithium ion transport in electrolyte

Due to lack of the proportion of the electrolyte components, the dynamic variables dependent on temperature of lithium ion transport in LiPF₆ are assumed to follow the properties of similar electrolyte systems. Valøen [32] investigated a full set of transport properties for LiPF₆ in PC/EC/DMC (10:27:63 by volume) experimentally, showing the k_2 , D_2 , and v as functions of temperature and LiPF₆ concentration.

$$D_2 = 1 \times 10^{-4} \times 10^{-4.43 - \frac{54.0}{T - 229.0 - 0.05C} - 2.2 \times 10^{-4}C} \quad (40)$$

$$v = 0.601 - 0.24\sqrt{10^{-3}C} + 0.982(1 - 0.0052(T - 294.0)\sqrt{10^{-9}C^3}) \quad (41)$$

$$k_2 = 1 \times 10^{-4} \left(-10.5 + 0.074T - 6.69 \times 10^{-5}T^2 + 6.68 \times 10^{-4}C - 1.78 \times 10^{-5}CT + 2.8 \times 10^{-8}CT^2 + 4.49 \times 10^{-7}C^2 - 8.86 \times 10^{-10}C^2T \right) \quad (42)$$

By combined the parameters of LiPF₆ in EC/DMC (2:1 by volume) at 25 °C [46] with that in the PC/EC/DMC system [32], the following expression is obtained:

$$k_2 = 1.12 \times 10^{-4} \left(-8.2488 + 0.053248T - 2.9871 \times 10^{-5}T^2 + 0.26235C - 9.3063 \times 10^{-3}CT + 8.069 \times 10^{-6}CT^2 + 0.22002C^2 - 1.765 \times 10^{-4}C^2T \right) \quad (43)$$

The Li⁺ transference number, t^+ , is considered as a constant, such as $t^+ = 0.363$ [14]. However, t^+ also appears to be dependent of Li⁺ concentration and temperature [47,48]. Hence, t^+ is adopted from the published literature [47,48] that is a function of temperature and Li⁺ concentration in this study.

$$t^+ = 2.67 \times 10^{-4} \exp\left(\frac{833}{T}\right) \left(\frac{C}{1000}\right) + 3.09 \times 10^{-3} \exp\left(\frac{653}{T}\right) \left(\frac{C}{1000}\right) + 0.517 \exp\left(-\frac{49.6}{T}\right) \quad (44)$$

It should be noted that the solvent mixture for the commercial battery is unknown. We assume that Eqs. (40)–(44) are applicable in commercial batteries, so, these data are used in this simulation.

3.3. Model validation

The electrochemical–thermal model is validated from electrochemical performance. Experiment data are from the introduction document of ANR26650m1-a lithium ion cylindrical cell (A123 company, US) [49].

Firstly, the experiment data [49] of battery potential against the discharge capacity are compared with simulation results that are in fairly good agreement with the experimental results (see Fig. 3). In order to further validate the electrochemical performance at different discharge rates, the simulation results are compared with the experiment data [25] at different discharge rates (C/10, 1/2C, 1C, 2C) at 25 °C in Fig. 4. The results indicate this electrochemical–thermal model based dynamic response is reliable to simulate the discharge performance of lithium iron phosphate battery at different discharge rates.

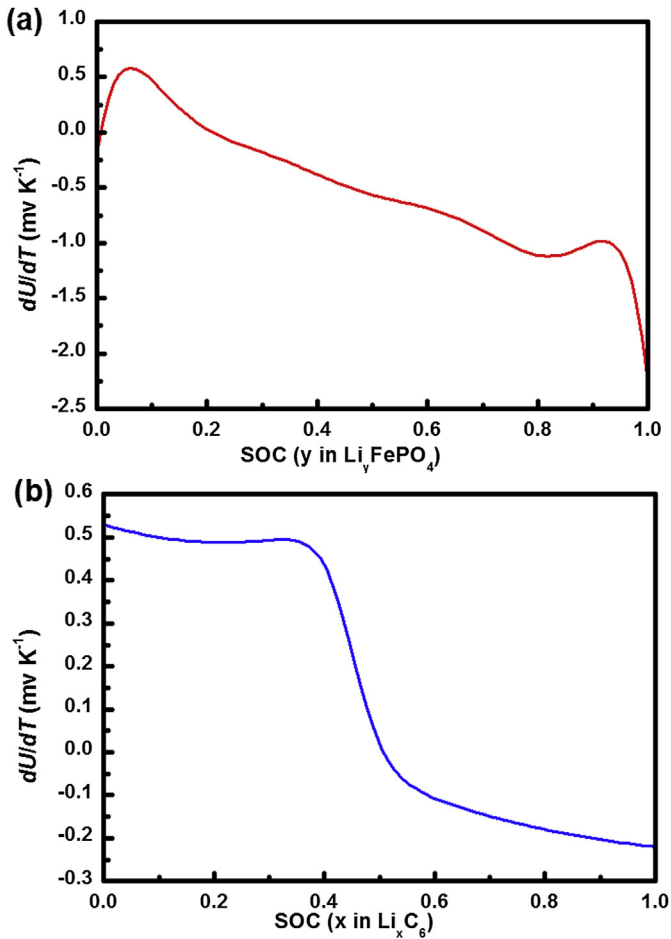


Fig. 2. The entropy change of the positive electrode and negative electrode as a function of SOC.

4. Results and discussion

This model is mainly used to predict the electrochemical performance and thermal behavior of lithium ion batteries.

4.1. Dynamic evolution for pulse behavior

Lithium ion batteries have been used in many aspects which work intermittently, for example, assisting the engine of hybrid electric vehicles during vehicle acceleration. Because these actions are of short duration, on the order of seconds, the pulse and relaxation behaviors are considered important aspects to analyze polarization in battery. In this study, pulse test with different discharge rates was chosen to obtain Li⁺ concentration distribution. During simulated operation, the battery is discharged at 0.2C, 1C, or 2C constant current during 0–200 s and is relaxed by cutting off current during 200–1000 s. The Boundaries 2, 3, 4 and 5 are used to examine the spatial and temporal distribution of lithium ion concentration in liquid and solid phases.

The spatial and temporal distribution of lithium ion concentration in electrolyte (c_2) during the pulse test at different discharge rates is depicted in Fig. 5. At the beginning of the discharge, a distribution of lithium ion rapidly builds up inside the battery, c_2 decreases from Boundary 2 to Boundary 5, forming a gradient which drives lithium ions along the battery direction from the negative electrode to positive electrode. At a high discharge rate (1C or 2C), c_2 increases in the negative electrode and decreases in the

positive electrode during the very early period (about 80 s), and then stays steady from 80 s to 200 s. On the contrary, at a low discharge rate, c_2 changes from 0 s to 200 s. When the current is cut down at 200 s, c_2 changes rapidly in a timescale of millisecond. Then a self-adjusting period driven by diffusion is taken to attain equilibrium. The greater discharge rate is, the longer self-adjusting period. Due to the employment of double layer capacitance of the active materials and electrolyte interface, c_2 in equilibrium shows an increase compared to the initial level (1200 mol m^{-3}). At 0.2, 1 and 2C discharge rates, the augmentation is $0.6, 8.4, 9.9 \text{ mol m}^{-3}$, respectively, showing a rising trend along with an increase of the discharge rates. However, this rising is not obvious at high discharge rates.

Lithium ion concentration gradient in solid phase can be described as an indicator of polarization in a particle. Large concentration gradient in a solid particle means high polarization, which may lead to high diffusion induced stress (DIS), cause particle fracture and reduce battery capacity and battery power [50]. As introduced in the section of model development, active materials (LiFePO₄ and Graphite) in solid electrodes are considered to be homogenous, and they are composed of spherical particles. In order to study their interior lithium ion concentration gradient, four special particles at Boundary 2, 3, 4 and 5, respectively, are selected, and they divided into 10 parts along the radial direction. The center and surface of the particles are located at $r/R = 0$ and 1, respectively. Fig. 6 gives lithium ion concentration distribution throughout the particles.

At all of the boundaries, lithium ion concentrations of the particles show great changes at pulse time of 0–200 s. They decrease at Boundary 2 and 3 in the negative electrode with discharge time, as shown in Fig. 6a and b. However, an increase with discharging time at Boundary 4 and 5 in the positive electrode is seen in Fig. 6c and d. At 200 s, the surface concentrations of particles at Boundary 2 and 3 decrease to 25.2 kmol m^{-3} and 24.3 kmol m^{-3} , from initial concentration ($26.98 \text{ kmol m}^{-3}$), and at Boundary 4 and 5 the concentrations increase to 2.3 kmol m^{-3} and 1.7 kmol m^{-3} from initial concentration (0.5 kmol m^{-3}). These indicate the lithium ion distribution is in location dependent.

After the current is cut down at 200 s, the battery is in relaxation. In the relaxation period (200–1000 s), the variation of lithium ion concentration in the negative electrode including Boundary 2 and 3 appears the similar tendency. At $r/R_n = 0, 0.1, 0.2, 0.3, 0.4$, the concentrations decrease gradually until unchanged. And at $r/R_n = 0.5, 0.6, 0.7, 0.8, 0.9, 1.0$ the concentrations turn to increase until unchanged. As for the positive electrode, the variation of

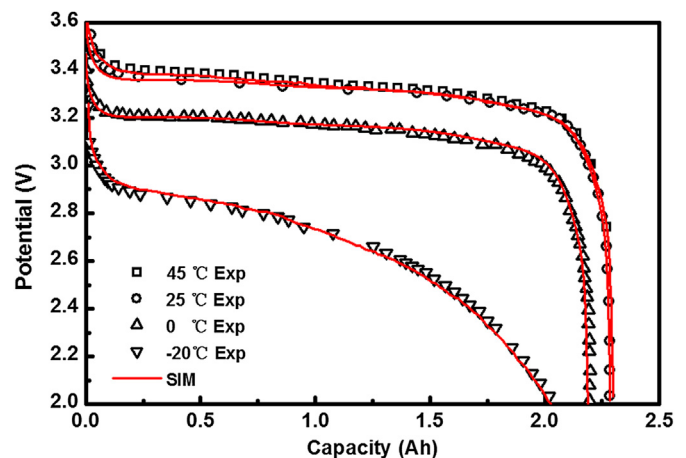


Fig. 3. -20 °C, 0 °C, 25 °C, 45 °C, 1C discharge validations.

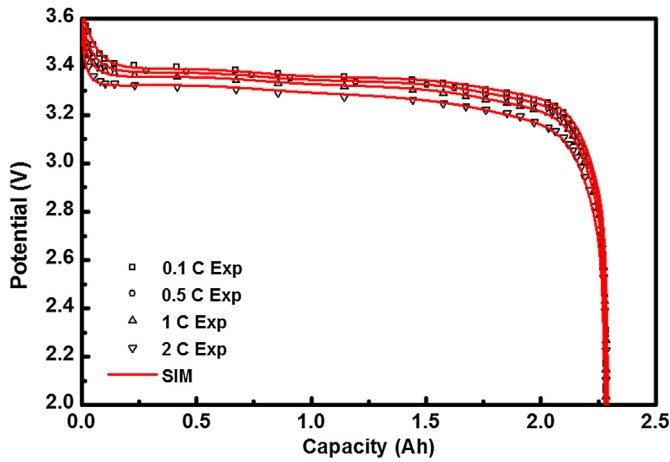


Fig. 4. Different discharge rates (0.1C, 0.5C, 1C, 2C) validation at 25 °C.

interior lithium ion concentration of the particle at Boundary 5 shows a contrary location dependent with Boundary 2 and 3. At $r/R_p = 0, 0.1, 0.3, 0.2, 0.4$, the concentrations continue increasing gradually until unchanged, and at $r/R_p = 0.5, 0.6, 0.7, 0.8, 0.9, 1.0$ the concentrations turn to decrease until unchanged. But for Boundary 4, lithium ion concentrations of the particle decrease gradually until unchanged, appearing no location dependence that is quite different from at other boundaries.

In the relaxation period, the interior concentrations remain unchanged ultimately, which is in equilibrium. It is well known that the cells of a battery require a certain time to reach a steady state in terms of charge, concentration and temperature. As introduced in literature [51], relaxation time factor (R^2/D) denotes the theory time needed for interior concentrations to obtain equilibrium after pulse discharge, which reflects the depolarization ability of the battery. In theory, at 25 °C, $R_n^2/D_n = 136$ s, and

$R_p^2/D_p = 1129$ s. With the discharge proceeding, battery temperature will increase that leads to D increase (see Eqs. (32) and (33)). So R^2/D at discharge process is lower than that at 25 °C. That explains why the relaxation times of negative and positive electrodes concluded from Fig. 6 (about 120 s and 370 s) are lower than theoretical values. Increasing lithium ion diffusivity in solid phase may decrease the polarization and improve the relaxation performance of battery.

Besides, Fig. 7 shows the potential in solid phase also changes at pulse test. The potential decreases with time as a typical saw-tooth behavior, corresponding to the increase of lithium ion concentration on the surface of positive particle (Fig. 6c and d). Within 200 s, the voltage decrease at boundary 5 that is larger than that at boundary 4 due to the ohmic overvoltage contributed from the thickness of positive electrode. The relaxation of the potential after current interruption occurs in two stages. When the current is cut down at 200 s, the decrease is also shut down immediately. And the potential increases by 0.04 V quickly with a timescale less than 0.2 s, which is caused by the disappearance of ohmic polarization. Duo to the diffusion of lithium ions, the potential increases slowly until equilibrium is attained.

4.2. Dynamic evolution for electrochemical reaction

In order to observe the dynamic evolution in the electrodes, the local current density, surface concentration and the state of charge are simulated. The curves of these properties at different time during discharge are shown in Figs. 8 and 9. In the negative electrode (Fig. 8a), the local current density does not change in regularity. For the positive electrode, the local current density at Boundary 4 increases severely at the beginning of discharge. A peak is seen at 1220 s in the local current density curve, and it moves from the separator-positive electrode interface to the positive electrode-current collector interface. This indicates large electrochemical reaction rate near the separator-negative electrode

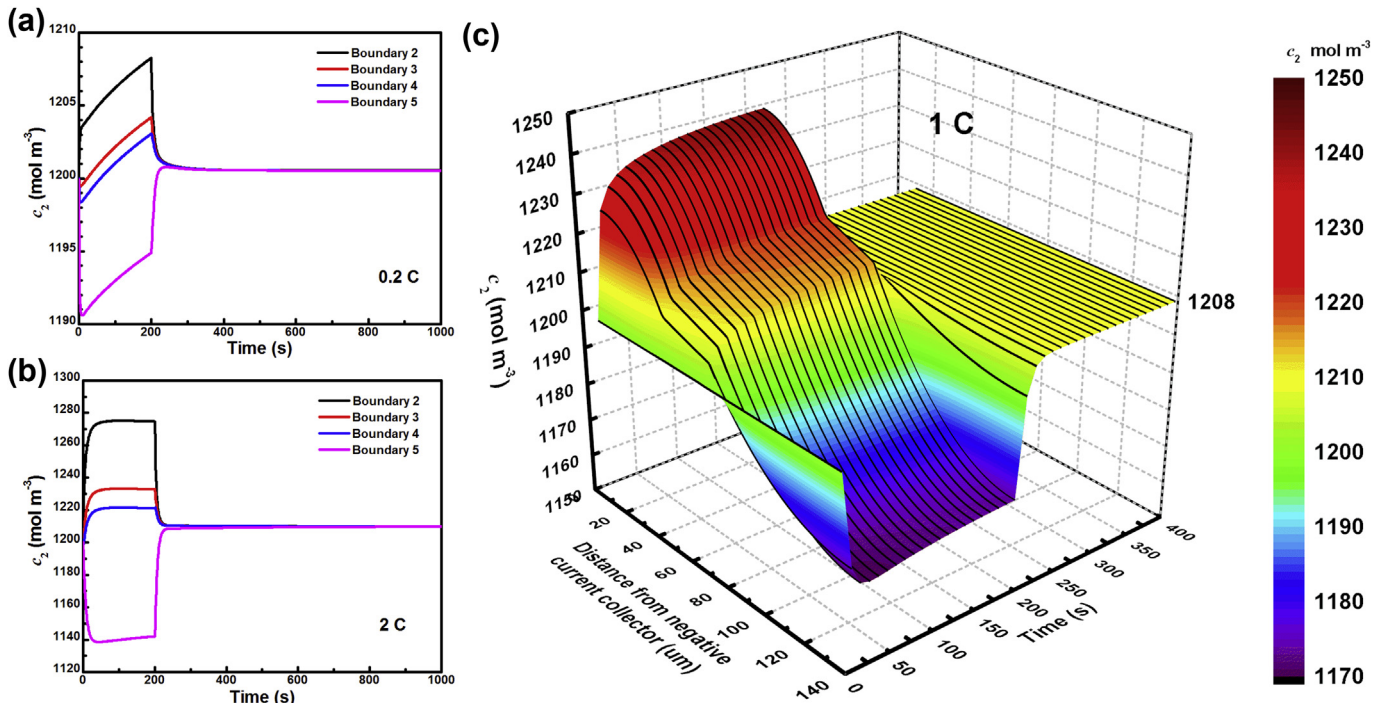


Fig. 5. Spatial and temporal distribution of Li^+ concentration in electrolyte.

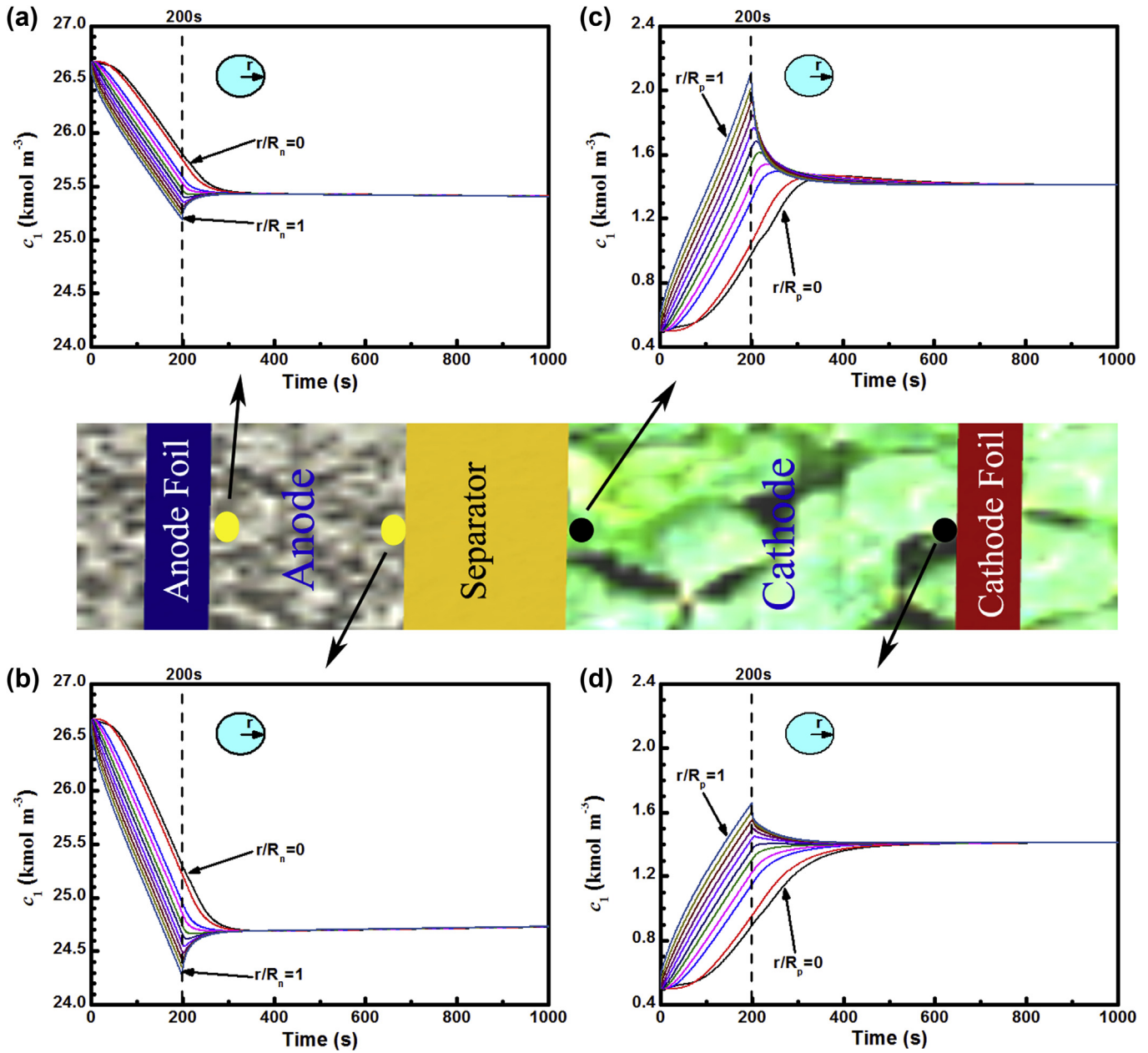


Fig. 6. Li^+ distribution along particle radius during pulse tests (boundary 2, 3, 4 and 5).

interface. This result is different from the report of Wang and his co-works [22] in which the peak moved from the current collector to the cathode-separator interface as discharge proceeded. This is because the peak location depends upon the comparison between the effective conductivity of the solid phase (k_1^{eff}) and that of the liquid (k_2^{eff}) [51]. When $k_1^{\text{eff}} < k_2^{\text{eff}}$, the peak appears near the current collector and moves from the current collector to the cathode-separator interface as discharge proceeds. On the contrary, when $k_1^{\text{eff}} > k_2^{\text{eff}}$, the peak appears near the cathode-separator interface and moves from the cathode-separator interface to the current collector as discharge proceeds. In our work, k_1^{eff} is larger than k_2^{eff} , therefore, the surface concentration near the separator-positive electrode is increased rapidly to the maximum concentration of 22,806 mol m⁻³ as shown in Fig. 9a, and the positive particles approximately reach the fully state of charge in a short time (about 1800 s) (Fig. 9b).

The state of charge (SOC) is defined by the quotient of the surface concentration divided by the maximum concentration of 22,806 mol m⁻³. Therefore, the surface concentration and the state of charge distributions at different time represent the same as shown in Fig. 9. The particles near to the separator-positive electrode interface firstly approach the fully discharge state. As a consequence, the utilization of active materials is not the same. As the curve shown in Fig. 8b, the peak of the local current density at the end of discharge has not reached the positive electrode-current collector boundary at $t = 3577$ s. Correspondingly, the surface concentration in the region close to the current collector also has not reached the maximum concentration. In addition, the local state of discharge is far less than 1, which indicates that the active material is not adequately utilized. That is because the stop condition is determined by the cut-off voltage in both simulation and practice. When the cut-off voltage is reached, the utilization of

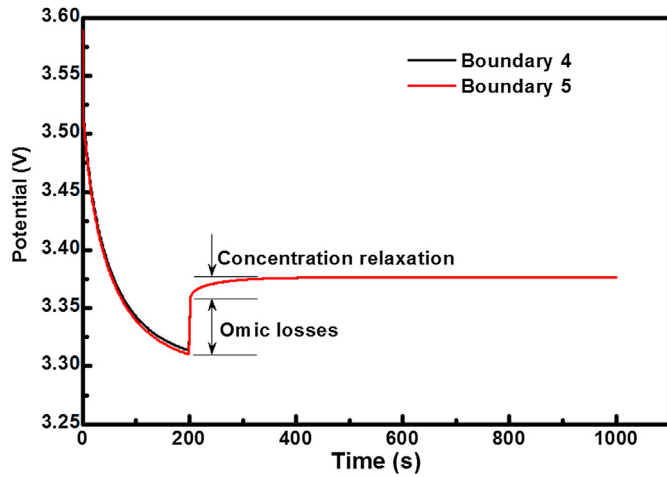


Fig. 7. Dynamic evolution for potential in solid phase during pulse tests (boundary 4 and 5).

active materials may not be 100%. To optimize battery design and achieve better performance, it is essential to choose appropriate values for some design parameters.

4.3. Heat generation and thermal behavior

Understanding the thermal behavior of these heat generation sources would offer much valuable information to develop the battery thermal management strategies. There are several heat generation mechanisms, as shown in Fig. 10. The overall heat generation of the battery discharge is consisted of electrochemical reaction heat, ohmic heat and active polarization heat produced in the negative electrode, electrolyte and positive electrode. The heat generations of negative and positive electrodes are complex, as shown in Table 1. The ionic ohmic and electrochemical interface heats are dominant contributor, nearly 100% of the total heat generation. The ionic ohmic heat from negative electrode is positive and nearly constant through the whole discharge except 0–25 s, which is mainly due to the rapid change of the ionic ohmic at early discharge. An S-shape change of the electrochemical interface heat is observed from negative to positive as a function of time. Its shape resembles a mirror image of the entropy change versus SOC curve

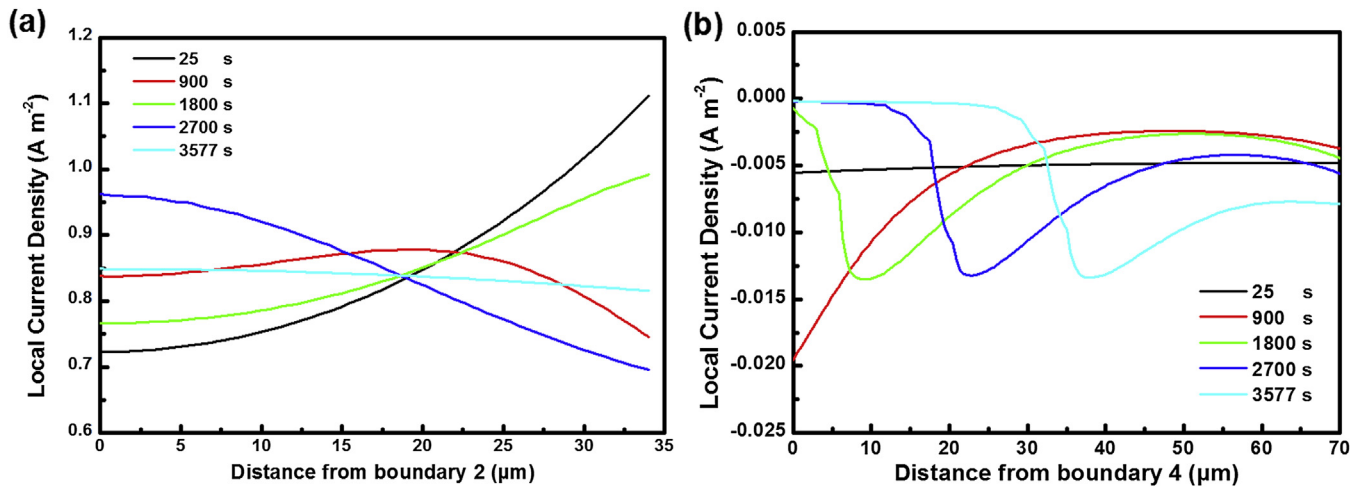


Fig. 8. The local current density distributions at different time during the discharge at 1C rate. (a) The negative electrode side and (b) the positive electrode side.

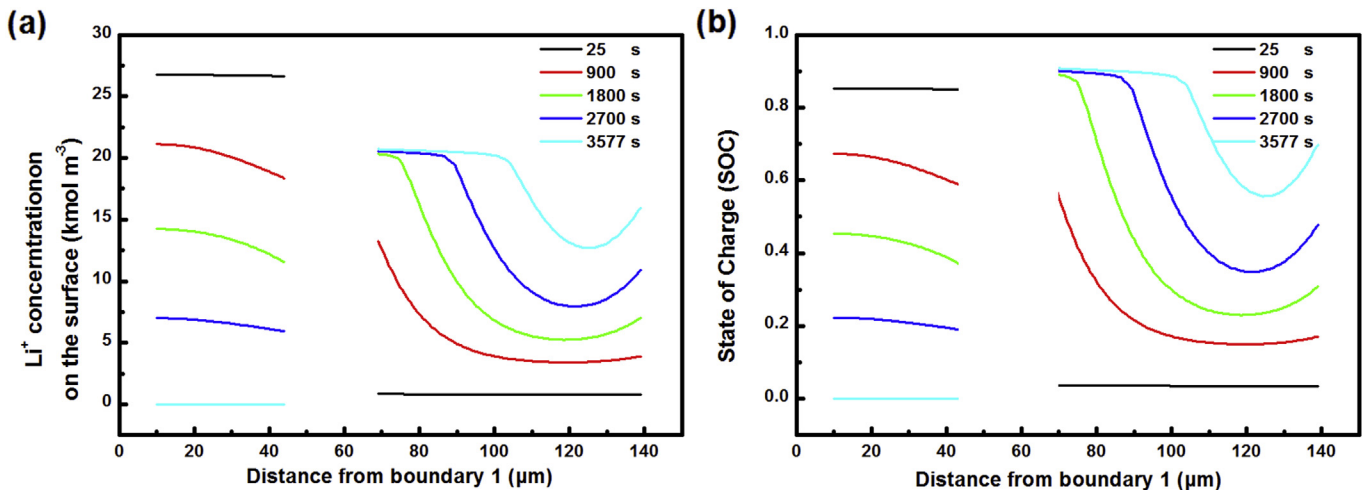


Fig. 9. The state of charge distribution at different time during the discharge at 1C discharge.

of the Li_xC_6 anode in Fig. 2a. Due to the electrochemical interface heat, the total heat generation rate of negative electrode also exhibits an S shape.

As shown in Fig. 10b, the value of ionic ohmic heat from positive electrode is also positive through the whole discharge progress. But it appears a large range, which illustrates that the ionic ohmic of positive electrode is more variable than the negative electrode. With the combined effects of ionic ohmic heat and electrochemical interface heat, the total heat of the positive electrode does not exhibit the shape as the entropy of the positive electrode change versus SOC curve of the LiFePO_4 cathode in Fig. 2b. Compared to the heat generation of porous electrodes, the heat generation of the current collectors and separator are tiny and can be neglected, as shown in Fig. 10c and d.

As introduced in the part of energy balance, the heat generation can be divided into two types, irreversible heat and reversible heat. The heat generation of the current collectors and separator shown in Fig. 10c and d is irreversible joule heat. Fig. 11 plots the irreversible heat, reversible heat and the total heat of porous electrodes and the battery system. Comparing Eqs. (19), (24) with Eq. (26), we obtain the relation as Eq. (45), which means that the electrochemical interface heat of porous electrodes comprises reversible heat generation and active heat generation. The curve of the reversible heat in Fig. 11a almost has the same shape with the curve of electrochemical interface heat in Fig. 10a, except the time range from 1450 s to discharge end. From the value and shape difference,

we can deduce that the active heat generation of negative electrode is about $5 \times 10^4 \text{ W m}^{-3}$ and have a server increase from 1450 s to the discharge end. And the active heat generation of the positive electrode remains a stable value of $2 \times 10^4 \text{ W m}^{-3}$. The active heat generation, also called polarization heat generation, is directly dependent on the overpotential, so we can conclude that the variation of the overpotential in negative electrode is severer than in positive electrode, especially at the last stage of discharge. The negative electrode plays an important role for the contribution to the overpotential in a complete battery. The total heat generation of the negative electrode is slightly higher than that of the positive electrode. While the thickness of the positive electrode ($70 \mu\text{m}$) is more than twice that of the negative electrode ($34 \mu\text{m}$), so the heat generation of a complete battery come mostly from the positive electrode, which is the reason why the shape of the total heat generation is similar to that of the positive electrode, as shown in Fig. 11b and c.

$$\begin{aligned} q_{i,(1)} &= S_{a,i} j_{\text{loc},i} \left(T \frac{dU_i}{dT} + \phi_{1,i} - \phi_{2,i} - U_i \right) \\ &= \left(Q_{\text{rea}} = S_{a,i} j_{\text{loc},i} T \frac{dU_i}{dT} \right) \\ &\quad + [Q_{\text{act}} = S_{a,i} j_{\text{loc},i} (\phi_{1,i} - \phi_{2,i} - U_i)] \end{aligned} \quad (45)$$

As shown in Fig. 11, the reversible heat accompanied endothermic process and exothermic process, and the irreversible

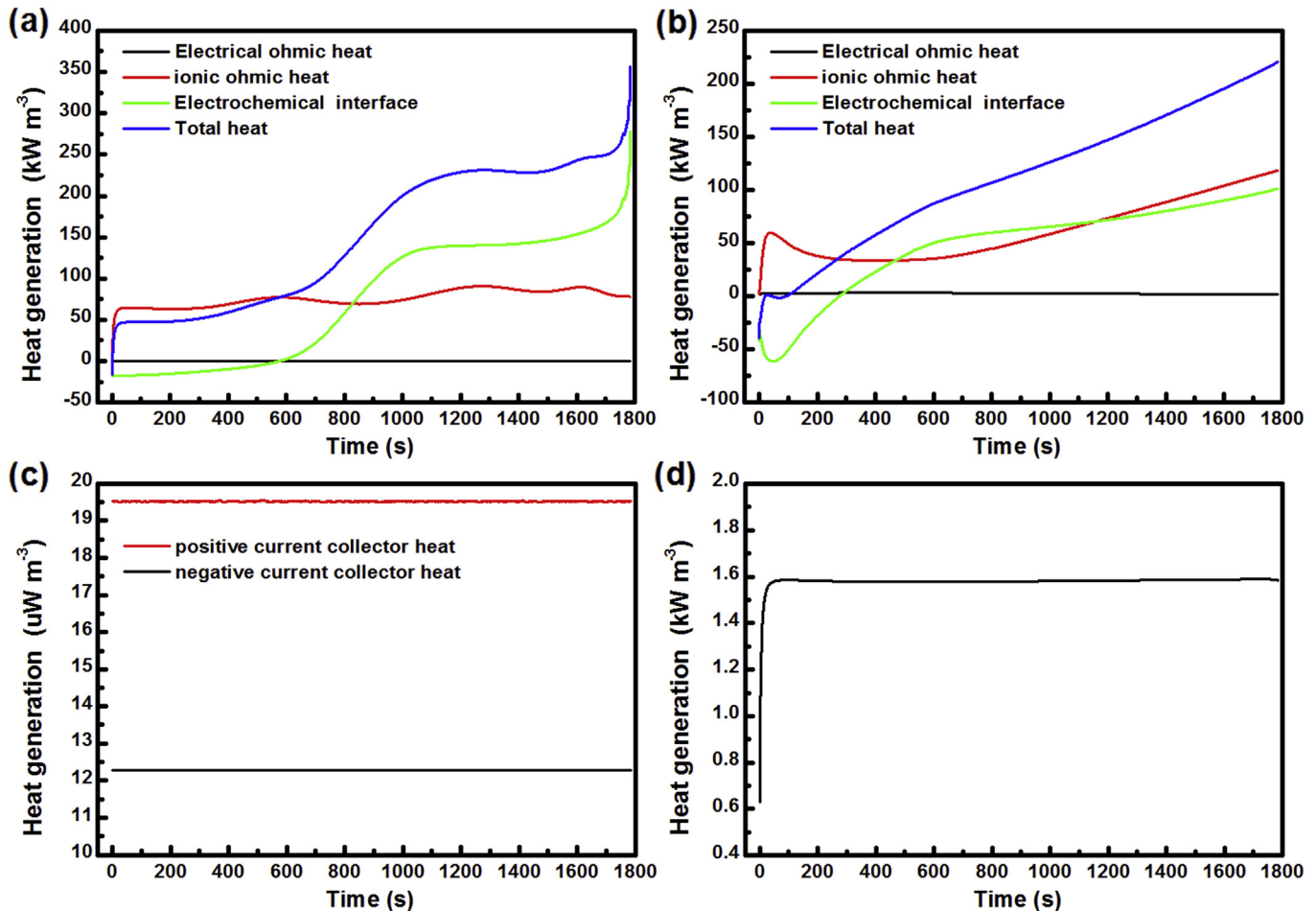


Fig. 10. Time history of heat generation by various mechanisms during discharge at 2C rate. (a): negative electrode; (b): positive electrode; (c): current collectors; (d): separator.

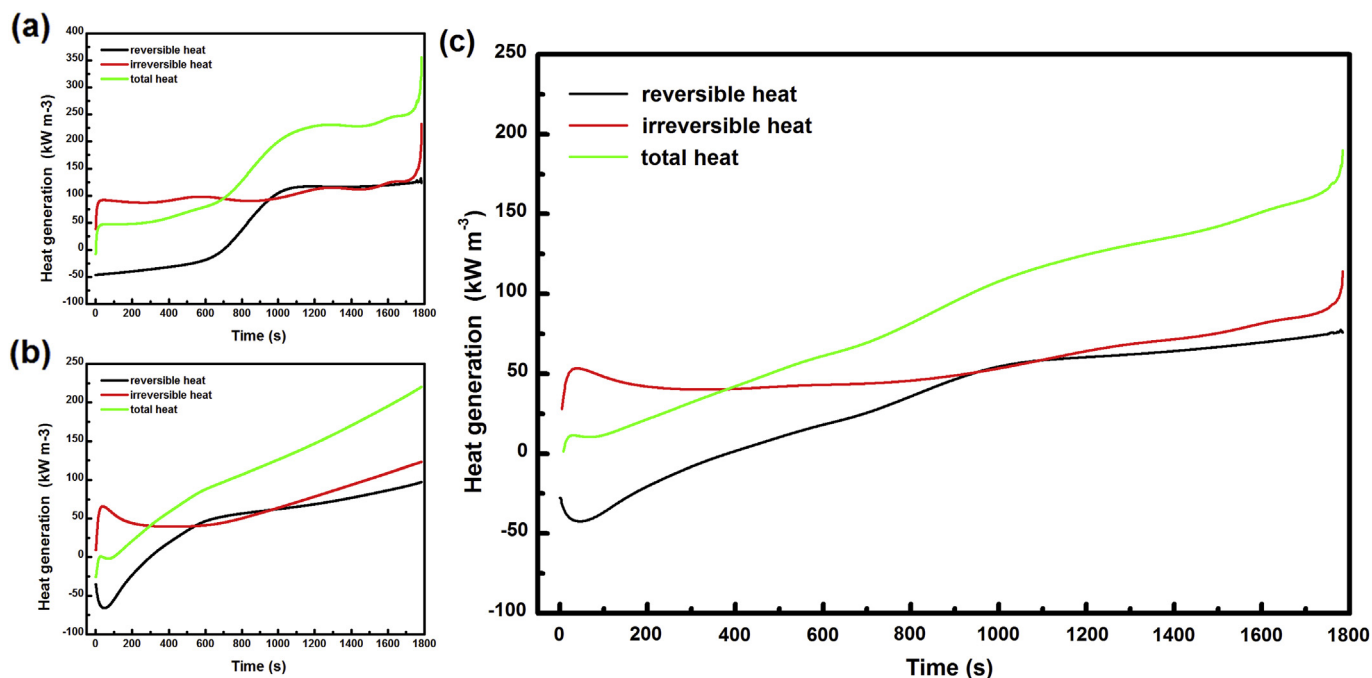


Fig. 11. Time history of reversible and irreversible heat generation during discharge at 2C rate. (a): Negative electrode; (b): positive electrode; (c): complete battery.

heat is exothermic progress and increases with increasing the discharge rate [52]. Their combination determines whether the discharge process is exothermic or not. Fig. 12 shows the total heat generation of complete battery at different discharge rate. The blue (in the web version) area stands for the endothermic heat, the red area represents the exothermic heat with an equal amount of the blue area, and the yellow area represents the net heat. At low discharge rate like 0.5C, the discharge electric current is so small that the polarization is not serious, which leads smaller exothermic amount of irreversible heat than the endothermic amount of reversible heat. Hence, there are three colored areas existing in Fig. 12a, indicating the discharge process of the LiFePO₄ battery is accompanied exothermic and endothermic processes at low rates. The same phenomena still exists in 1C discharge process. But when the rate is increased to 2C and above, only yellow area is left, indicating only exothermic phenomena existing. This phenomenon is in a good agreement with the experimental work of Liubin Song and his coworkers [53,54]. Fig. 13a shows evolutions of the average battery temperature during 1C discharging. The battery is surrounded by natural air at 25 °C. At the initial stage of discharge, the average temperature increases slowly. But, the average temperature increases to about 37 °C at the end of discharge. Fig. 13b is the contour plot of the battery temperature distribution at the end of 1C discharging. Hot area is distributed at the axial core of the battery. Due to larger thermal conductivity in the axial direction, the temperature distribution in this direction is uniform. The main temperature variation is in the radial direction with a value about 1.5 °C. Basing on the comparison between the heat generation of 5C and 1C in Fig. 12 and the temperature contour plot at 1C in Fig. 13, the battery temperature will reach more than 60 °C at 5C discharging rate. Appropriate rates can be used to avoid the internal heat accumulation of batteries.

All computations are carried out on a DELL PRECISION T1650 Workstation with two quad-core processors (Intel Core i7-3770, 3.4 GHz, with a total of eight processor cores) and a total of 16 GB random access memory (RAM).

5. Conclusion

In this paper, an electrochemical–thermal model based dynamic materials response for lithium iron phosphate battery is developed by employing the comprehensive dynamic parameters in thermodynamics and kinetics. The current collectors are considered in the model. This model is validated in aspects of electrochemical performance, thermal performance, which is in a good agreement between the simulated results and experimental results.

The pulse tests show that the self-adjusting period needed for lithium ion concentration in electrolyte to attain equilibrium after relaxation is affected by the discharge rate. The greater discharge rate is, the longer self-adjusting period. Because the rate of lithium ions deintercalating from the negative porous electrode is larger than that of intercalating into the positive electrode, after enough relaxation, the lithium ion concentration in electrolyte shows an augmentation compared to initial level. And the self-adjusting period needed for lithium ion concentration in particle to attain equilibrium is longer than that for electrolyte. The existence of critical makes the dynamic evolution for lithium ion concentration in solid phase much complicated. Moreover, in constant current discharge processes, the electrochemical reaction rate is location-related, and the maximum rate moves from the separator-positive electrode interface to the positive electrode-current collector interface, resulting the utilization of active material is not uniform. At the end of discharge, there is still a part of the active material has not been adequately utilized. The discharge process of LiFePO₄ battery accompanied exothermic process and endothermic process at a low rate. With the rate increasing, the endothermic phenomena disappears gradually, the heat production rate and the enthalpy change during the discharge process of LiFePO₄ battery increase. When the rate is increased to 2C, only exothermic phenomena exists. These suggest that appropriate rates for batteries should be chosen in order to avoid safety problem.

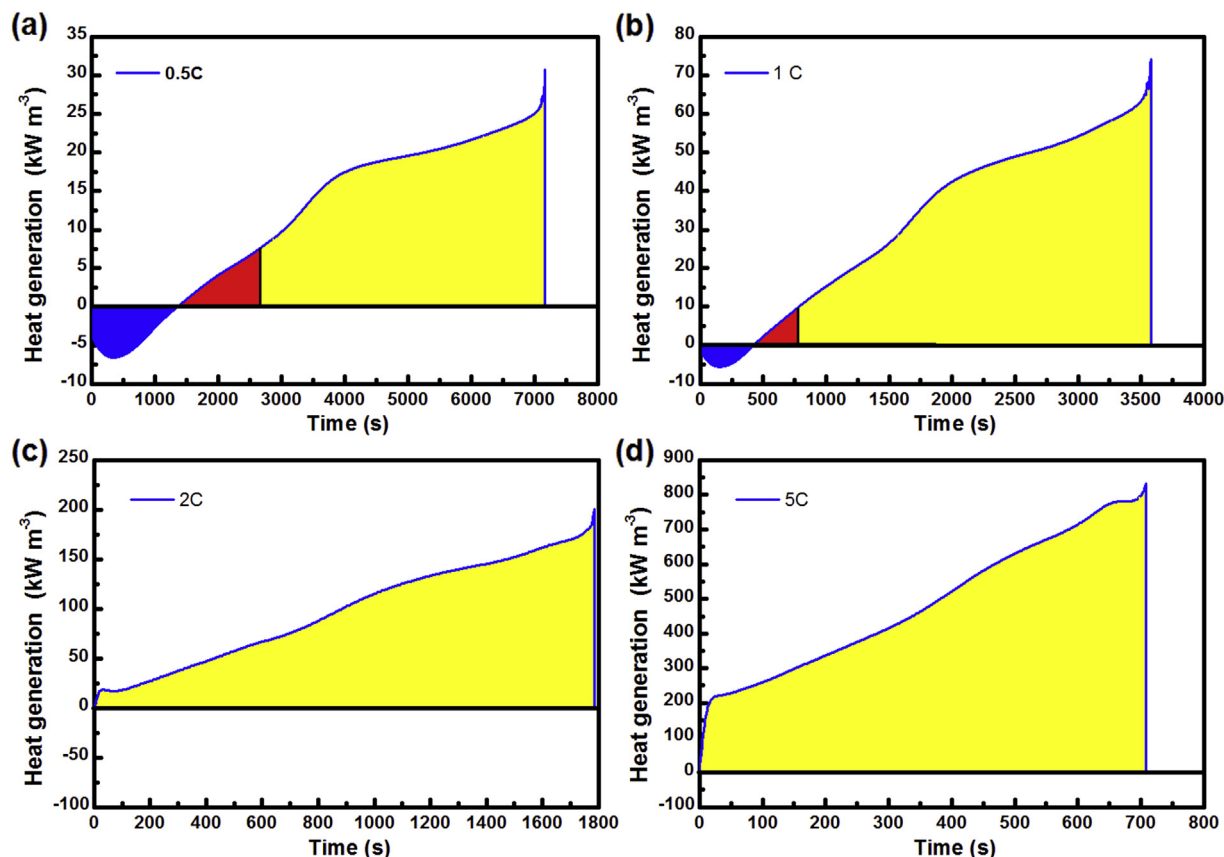


Fig. 12. The total heat generation of complete battery at different discharge rate.

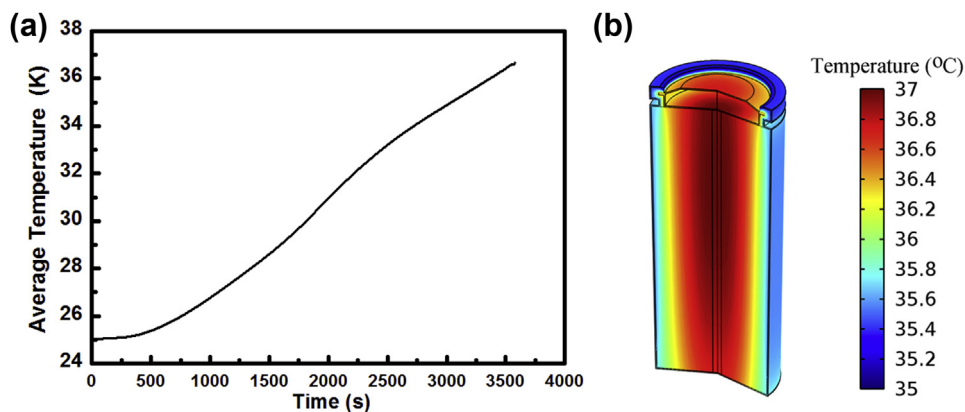


Fig. 13. (a) Evolutions of the average battery temperature during 1C discharging and (b) the contour plot of the battery temperature distribution at the end of 1C discharging.

Acknowledgment

This work is supported by funds from the National Natural Science Foundation of China (No. 51204211), the China Postdoctoral Science Foundation (No. 2012M521543) and the Specialized Research Fund for the Doctoral Program of Higher Education of China (No. 20120162120089). The assistance from Prof. Jin Liu in manuscript polishing is also greatly appreciated.

References

- [1] B. Scrosati, J. Garche, *J. Power Sources* 195 (2010) 2419–2430.
- [2] J. Wang, X. Sun, *Energy Environ. Sci.* 5 (2012) 5163–5185.
- [3] T. Reddy, *Linden's Handbook of Batteries*, 2011.
- [4] K.-j. Lee, K. Smith, A. Pesaran, G.-H. Kim, *J. Power Sources* 241 (2013) 20–32.
- [5] Y. Tang, M. Jia, Y. Cheng, K. Zhang, H. Zhang, J. Li, *Acta Phys. Sin.* 62 (2013) 158201-1–158201-10.
- [6] A.A. Franco, *RSC Adv.* 3 (2013) 13027–13058.
- [7] W.B.J. Zimmerman, *Process Modelling and Simulation with Finite Element Methods*, 2004.
- [8] M. Doyle, T.F. Fuller, J. Newman, *J. Electrochem. Soc.* 140 (1993) 1526–1533.
- [9] T.F. Fuller, M. Doyle, J. Newman, *J. Electrochem. Soc.* 141 (1994) 1–10.
- [10] C.R. Pals, J. Newman, *J. Electrochem. Soc.* 142 (1995) 3274–3281.
- [11] C.R. Pals, J. Newman, *J. Electrochem. Soc.* 142 (1995) 3282–3288.
- [12] J. Yi, U.S. Kim, C.B. Shin, T. Han, S. Park, *J. Power Sources* 244 (2013) 143–148.
- [13] L. Cai, Y. Dai, M. Nicholson, R.E. White, K. Jagannathan, G. Bhatia, *J. Power Sources* 221 (2013) 191–200.
- [14] Y. Ye, Y. Shi, N. Cai, J. Lee, X. He, *J. Power Sources* 199 (2012) 227–238.

- [15] K. Somasundaram, E. Birgersson, A.S. Mujumdar, *J. Power Sources* 203 (2012) 84–96.
- [16] S. Elul, Y. Cohen, D. Aurbach, *J. Electroanal. Chem.* 682 (2012) 53–65.
- [17] S. Santhanagopalan, Q. Guo, P. Ramadass, R.E. White, *J. Power Sources* 156 (2006) 620–628.
- [18] L. Cai, R.E. White, *J. Power Sources* 196 (2011) 5985–5989.
- [19] A.K. Padhi, K.S. Nanjundaswamy, J.B. Goodenough, *J. Electrochem. Soc.* 144 (1997) 1188–1194.
- [20] A. Yamada, Y. Kudo, K.-Y. Liu, *J. Electrochem. Soc.* 148 (2001) A1153–A1158.
- [21] V. Srinivasan, J. Newman, *J. Electrochem. Soc.* 151 (2004) A1517–A1529.
- [22] M. Wang, J. Li, X. He, H. Wu, C. Wan, *J. Power Sources* 207 (2012) 127–133.
- [23] Y. Ye, Y. Shi, A.A.O. Tay, *J. Power Sources* 217 (2012) 509–518.
- [24] R.E. Gerver, J.P. Meyers, *J. Electrochem. Soc.* 158 (2011) A835–A843.
- [25] C. Hellwig, S. Sorgel, W.G. Bessler, *ECS Trans.* 35 (2011) 215–228.
- [26] V. Ramadesigan, P.W.C. Northrop, S. De, S. Santhanagopalan, R.D. Braatz, V.R. Subramanian, *J. Electrochem. Soc.* 159 (2012) R31–R45.
- [27] M. Safari, C. Delacourt, *J. Electrochem. Soc.* 158 (2011) A63–A73.
- [28] M. Safari, C. Delacourt, *J. Electrochem. Soc.* 158 (2011) A562–A571.
- [29] M. Safari, C. Delacourt, *J. Electrochem. Soc.* 158 (2011) A1436–A1447.
- [30] M. Safari, C. Delacourt, *J. Electrochem. Soc.* 158 (2011) A1123–A1135.
- [31] C. Delacourt, M. Safari, *J. Electrochem. Soc.* 159 (2012) A1283–A1291.
- [32] L.O. Valøen, J.N. Reimers, *J. Electrochem. Soc.* 152 (2005) A882–A891.
- [33] W. Wu, X. Xiao, X. Huang, *Electrochimica Acta* 83 (2012) 227–240.
- [34] M. Guo, G.-H. Kim, R.E. White, *J. Power Sources* 240 (2013) 80–94.
- [35] I.J. Ong, J. Newman, *J. Electrochem. Soc.* 146 (1999) 4360–4365.
- [36] L. Rao, J. Newman, *J. Electrochem. Soc.* 144 (1997) 2697–2704.
- [37] W.B. Gu, C.Y. Wang, *J. Electrochem. Soc.* 147 (2000) 2910–2922.
- [38] G.-H. Kim, A. Pesaran, R. Spotnitz, *J. Power Sources* 170 (2007) 476–489.
- [39] V. Srinivasan, J. Newman, *Electrochem. Solid-State Lett.* 9 A110–A2006.
- [40] D. Morgan, A. Van der Ven, G. Ceder, *Electrochem. Solid-State Lett.* 7 (2004) A30–A32.
- [41] D. Bernardi, E. Pawlikowski, J. Newman, *J. Electrochem. Soc.* 132 (1985) 5–12.
- [42] O.Y. Egorkina, A.M. Skundin, *J. Solid State Electrochem.* 2 (1998) 216–220.
- [43] T.L. Kulova, A.M. Skundin, E.A. Nizhnikovskii, A.V. Fesenko, *Russ. J. Electrochem.* 42 (2006) 259–262.
- [44] V. Srinivasan, C.Y. Wang, *J. Electrochem. Soc.* 150 (2003) A98–A106.
- [45] J.L. Dodd, Ph.D. Dissertation, California Institute of Technology, 2007.
- [46] J. Newman, W. Tiedemann, *AIChE J.* 21 (1975) 25–41.
- [47] G.-H. Kim, K. Smith, J. Ireland, A. Pesaran, *J. Power Sources* 210 (2012) 243–253.
- [48] M. Guo, R.E. White, *J. Power Sources* 221 (2013) 334–344.
- [49] http://www.akukeskus.ee/anr26650m1a_datasheet_april_2009.pdf.
- [50] C. Lim, B. Yan, L. Yin, L. Zhu, *Electrochimica Acta* 75 (2012) 279–287.
- [51] D.M. Bernardi, J.-Y. Go, *J. Power Sources* 196 (2011) 412–427.
- [52] V.V. Viswanathan, D. Choi, D. Wang, W. Xu, S. Towne, R.E. Williford, J.-G. Zhang, J. Liu, Z. Yang, *J. Power Sources* 195 (2010) 3720–3729.
- [53] L. Song, X. Li, Z. Wang, H. Guo, Z. Xiao, F. Zhang, S. Peng, *Electrochimica Acta* 90 (2013) 461–467.
- [54] L. Song, X. Li, Z. Wang, X. Xiong, Z. Xiao, F. Zhang, *Int. J. Electrochem. Sci.* 7 (2012) 6571–6579.